

Structural, Magnetic, Optical Properties and Photocatalytic Activity of Nanocrystalline Cobalt Ferrite Prepared by Three Different Methods

S. S. Selima (✉ samah_selima@yahoo.com)

Benha University <https://orcid.org/0000-0001-6884-2296>

W. A. Bayoumy

Benha University

M. Khairy

Benha University

M.A. Mousa

Benha University

Research Article

Keywords: CoFe₂O₄, Magnetic properties, Optical properties, Photocatalytic activity, Water treatment

Posted Date: March 5th, 2021

DOI: <https://doi.org/10.21203/rs.3.rs-271636/v1>

License: © ⓘ This work is licensed under a Creative Commons Attribution 4.0 International License. [Read Full License](#)

Abstract

Cobalt ferrite (CoFe_2O_4) nanoparticles were synthesized through three different routes (chemical co-precipitation, ceramic, and sol-gel). The products were characterized by XRD, SEM, TEM, Raman spectroscopy, FTIR, photoluminescence (PL), BET, XPS, vibrating sample magnetometer (VSM). The X-ray analysis validates the spinel structure of the samples with particle sizes between 21 – 36 nm. XPS revealed the impact of the preparation route on cation distribution at the tetrahedral and octahedral sites in spinel ferrite lattice. All ferrite surfaces exhibit a mesoporous structure with a surface area between 25 – 99 m^2/g . The results show that the prepared samples exhibit either ferromagnetic or super-paramagnetic behavior. The ferrite samples showed a photocatalytic performance under visible light. The present work demonstrates that each of the particle size and cation distribution is effective in controlling the structural, magnetic, and optical properties. The results obtained reveal that this kind of CoFe_2O_4 spinel ferrite nanoparticles has promising applications in magnetic designs and water treatment fields.

Introduction

Recently, magnetic nanoparticles have drawn an excessive arrangement of research due to their characteristic properties and their scientific, technological uses. Ferrite spinels consider as the most important class of these materials. The spinel structure exhibits a general formula $(\text{A})[\text{B}_2]\text{O}_4$ crystallizes in a face-centered cubic structure, with two lattice types for cation distributions of A and B sites in the tetrahedral and octahedral organization, respectively. The physical properties of ferrite spinel are linked to the cation distribution over the tetrahedral sites A (8a) and octahedral sites B (16d) of the structure. In practice, the spinel structure is more complex because molecules do not always correspond fully to a normal or inverse structure. Hence, an inversion parameter, d , defined by $0 < d < 1$ is introduced [1]. Cobalt ferrite is one of the most appropriate spinel ferrites which hold distinctive properties such as strong spin-orbit coupling, high coercivity, high Curie temperature, high magneto crystalline anisotropy, distinguished mechanical, and chemical stability [2-7]. Generally, cobalt ferrite exhibits a partially inverse spinel structure in which both sites (A and B) hold a fraction of Co^{2+} and Fe^{3+} cations and shows the formula of $(\text{Co}^{2+}_{1-d} \text{Fe}^{3+}_d)_\text{A}[\text{Co}^{2+}_d \text{Fe}^{3+}_{2-d}]_\text{B}\text{O}_4$ where d is a fraction of tetrahedral sites occupied by Fe^{3+} ions, which is known as the degree of inversion. The degree of inversion is sensitive to numerous parameters such as the microstructure and synthesis process. This work is designed to prepare CoFe_2O_4 with three different methods (co-precipitation, ceramic, and sol-gel) and investigate how the change in each of the cation distribution, particle size, and surface area affect the optical and magnetic properties, which ultimately determine the magnetic and photocatalytic applications.

Experimental

2.1. Materials

All chemicals were reagent grade and utilized without further purification. Cobalt (II) nitrate (Hexahydrate) $[\text{Co}(\text{NO}_3)_2 \cdot 6\text{H}_2\text{O}]$ was acquired from SD Finchem Limited, Mumbai 400 030. Ferric nitrate $[\text{Fe}(\text{NO}_3)_3 \cdot 9\text{H}_2\text{O}]$ was obtained from LOBA CHEMIE PVT.LTD. Cobalt (II) acetate $[(\text{CH}_3\text{COO})_2\text{Co} \cdot 4\text{H}_2\text{O}]$ was purchased from

Fluka, Garantie, Switzerland. Cobalt sulfate $\text{CoSO}_4 \cdot 7\text{H}_2\text{O}$ was prepared from the reaction of H_2SO_4 with CoCl_2 . Bidistilled water was utilized in all the experiments.

2. 2. Synthesis of CoFe_2O_4 Samples

CoFe_2O_4 nanoparticles were prepared by three different methods:

2.2.1 Ceramic Method

A mixture of $\text{CoSO}_4 \cdot 7\text{H}_2\text{O}$, $\text{Fe}(\text{NO}_3)_3 \cdot 9\text{H}_2\text{O}$, NaOH, and NaCl in the molar ratio of 1: 2: 8: 10 were pulverized together in an agate mortar for about 60 min., followed by calcination at 700°C for two hours. The obtained product was crushed and well washed with bidistilled water and dried at 95°C for one hour and heated to 700°C with a heating rate of $5^\circ\text{C}/\text{min}$. The sample was symbolized as CoFe_c .

2.2.2 Co-precipitation Method

Cobalt and iron nitrate, in a molar ratio of 1:2, were dissolved in bidistilled water. Urea was then added to the heated solution at 90°C with stirring. The precipitate obtained was filtered, well washed with bidistilled water, and dried at 95°C for 12 hours. Finally, the powder acquired was calcined up to 700°C with a heating rate of $5^\circ\text{C}/\text{min}$. The sample was denoted as CoFe_p .

2.2.3. Sol-Gel Method

A mixture of 2.91 g of $[\text{Co}(\text{NO}_3)_2 \cdot 6\text{H}_2\text{O}]$, 8.08 g of $[\text{Fe}(\text{NO}_3)_3 \cdot 9\text{H}_2\text{O}]$, and 10 g of citric acids were dissolved in bidistilled water with stirring at 85°C to get gel phase. The gel gained was then dried in an oven at 100°C for 12 hours. Finally, the powder obtained was calcined up to 700°C with a heating rate of $5^\circ\text{C}/\text{min}$. The sample was symbolized as CoFe_g .

2.3. Characterization Methods

XRD analysis was performed on a Philips X' Pert Pro Super diffractometer with Cu K α radiation ($\lambda=1.54 \text{ \AA}$). Electron microscope analysis was done by SEM and TEM electron microscopy model JEOL JEM-100CXII and JEOL-2010, respectively. The FT-IR spectra of the specimens were obtained by employing a Bruker-FT-IR in the range of $4000\text{-}400 \text{ cm}^{-1}$. A U-1000 laser Raman Spectrometer with 514.5 nm line of an ArC laser was used to determine Raman spectra. Optical absorption was measured by employing Cary 5G equipment, at wavelengths ranging from 200 to 1000 nm. The photoluminescence (PL) studies were made using a 225 nm excitation wavelength source. Traditional surface area and textural surface properties were studied using the BET- N_2 gas adsorption technique. The electron binding energies for the elements were determined using a PHI-5702 multifunctional spectrometer with AlK α radiation (XPS). The magnetic properties of the prepared samples were studied using the vibrating sample magnetometer model (VSM-9600M-1, USA) in a maximum applied field of 10 kOe.

A programmable ammonia desorption technique (TPD-NH₃) was used to determine the type and the amount of acidity in the studied samples. This is performed in a reactor filled with 0.4 g of the sample, which was previously activated at 250 °C for 3 hours with N₂ flow. The sample was then permitted to expose to NH₃ at room temperature for one hour. The overflow of NH₃ was swill out of the reactor with N₂ flow. The temperature was then elevated linearly at a rate of 10 °C/min to liberate NH₃ gas from the sample at a temperature interval of 100 °C up to 500 °C. The liberated NH₃ is allowed to flow through a known large amount of H₂SO₄ solution. Finally, the amount of acid was determined by back titration with NaOH solution using M.O indicator.

2.4. Photocatalytic Study

Basic Red 18 (BR 18) dye was selected as an ideal system for a catalytic reaction because of its intense color in an aqueous medium and low biodegradability due to the existence of benzene rings. The photocatalytic degradation of Basic Red 18 (BR 18) dye over ferrite nanoparticles was performed in a photoreactor with a total capacity of 0.5 L. The illumination source was a UV-C lamp (200-980 nm, 9 W, Philips) put in the internal quartz tube of the photoreactor. The impact of ferrite dosage on Basic Red 18 (BR 18) dye oxidation was examined by utilizing a dose of 0-0.05 g/l. The photocatalytic study was investigated at a pH range of 2-9 and initial dye concentration in the range of 50-200 ppm. The solution pH was regulated using NaOH or HCl. Specimens were removed from the arrangement at specific periods and centrifuged, and the concentration in the supernatant dye solution was then analyzed using UV-vis Spectrophotometer (a Cary 5G equipment).

Results And Discussion

3.1. Characterizations

XRD patterns of the prepared CoFe₂O₄ ferrites are shown in Fig.1. All the ferrite samples showed diffraction peaks at 2θ values 31.6°, 37.0°, 44.1°, 55.4°, 59.1° and 65.1° attributed to the reflection planes of (220), (311), (400), (422), (511) and (440), respectively, of the spinel crystal structure (JCPDS 22-1086). No other peaks are observed for all specimens indicating the purity of the ferrites. There is a slight shift of (311) peak towards lower angle side in the order CoFe_s > CoFe_p > CoFe_g. The average lattice constant (a) for the (311) plane was determined using equation (1) [8] and the results obtained are listed in Table 1.

$$a = \sqrt{h^2 + k^2 + l^2} / 2 \sin\theta \quad (1)$$

Where "h k l" are miller indices. It is noted that the lattice constant follows the order: CoFe_s > CoFe_p > CoFe_g. This may be attributed to that a certain number of Co²⁺ ions (0.78 Å) transfer from octahedral sites, accompanied by opposite migrate of equivalent number of Fe³⁺ ions (0.645 Å) from tetrahedral to octahedral sites to relax the compressive strain. The average crystallite sizes (D_{XRD}) of the investigated samples were calculated (based on 3 different peaks) from the widening of reflection peaks using the Scherrer formula [7]:

$$D_{XRD} = 0.9 \lambda / \beta \cos\theta \quad (2)$$

Where λ is the X-ray wavelength and β is the half peak width of the diffraction peak in radiant. The results are listed in Table 1 and found to lie in the range of 21 – 33 nm. The average X-ray density (ρ_x) of the cobalt ferrite nanoparticles was determined using the following equation:

$$\rho_x = 8M/Na^3 \quad (3)$$

Where M is the molecular weight of cobalt ferrite, N is Avogadro's number. The results are also listed in Table 1.

The formation of the CoFe_2O_4 spinel structure was also supported by infrared spectra shown in Fig.1S. The spectra of all samples demonstrate two specific bands for spinel structure, ν_1 in the range $581\text{--}563\text{ cm}^{-1}$, relates to $M_{\text{tetr}}\text{-O}$ vibration at the tetrahedral site, and ν_2 in the range $428\text{--}402\text{ cm}^{-1}$ attributed to $M_{\text{octa}}\text{-O}$ vibration at the octahedral sites [9-11]. The mean feature bands observed are recorded in Table 1. The variation in the band positions is due to the difference in the metal–O distances for the octahedral and tetrahedral complexes referring to a change in cation distribution in the spinel structure by changing the preparation method. These results strongly support the results of XRD data. The broad bands focused at $1640\text{--}1625\text{ cm}^{-1}$ are appointed to the δ H-O-H bonding mode of the adsorbed water [12].

The SEM and TEM micrographs of the as-synthesized CoFe_2O_4 particles are given in Figs.2 (a and b). As seen, depending on the preparation method the nano-particles have been developed in different orders and clusters. SEM and TEM images of CoFe_s show morphology nanoparticles predominated by nanorods structure. The other cobalt ferrite specimens, CoFe_p and CoFe_g , demonstrates aggregated spherical particles besides particles with polygon morphologies. The variation in the morphology of the NPS shown in Figure 2.b denotes that the crystal growth of CoFe_2O_4 depends to a large extent on the preparation method. The nanoparticle sizes were obtained using histograms of 100 particles observed in the TEM image are listed in Table 1. The slight contrast found in the results of XRD and TEM is due to the different handles of the two tools. TEM analysis offers a number-average size distribution, XRD manifests a volume -averaged median size. In XRD, the correctness of Scherrer's formula is influenced by numerous variables, for example, diffraction line width, and surface tension. Thus, Scherrer's equation might cause particular errors in determining the fixed value of the crystallite size [7].

XPS results of the CoFe_2O_4 samples are given in Fig. 3, where binding energy (B.E.) ranges from 0 to 1200 eV. The spectra show that the samples contain only the main elements: Fe, Co, and O beside the contaminated C element coming from the environment. The binding energy (B.E.) values obtained attached well with the literature data for CoFe_2O_4 , Table 2, [13] proving that pure ferrite had been produced.

To investigate the cation valence states and their distribution in the CoFe_2O_4 spinel, the high-resolution XPS spectra of Fe 2p, Co 2p, and O1s peaks of the CoFe_2O_4 specimen were studied and given for CoFe_g in Fig. 4. The integrated intensities of the fitted peaks of Co^{2+} and Fe^{3+} ions were used to determine their distributions in both octahedral and tetrahedral positions. The table also shows an increase in the concentration of Fe^{3+} cations on octahedral sites with the increase in the particle size of the sample, which agrees well with XRD data. In conclusion, it can be said that the selection of the preparation route is effective in controlling the

cation distribution within the spinel lattice. The presence of high intense satellite structure on the high binding energy side of the Co 2p^{3/2} and Fe 2p^{3/2} might be attributed to the band structure related to octahedral Co 2p in the oxide lattice.

3.2. Magnetic Study

In order to investigate the effect of synthetic method on the magnetic properties, the VSM test was done at room temperature in an applied field of 10 kOe. The results are represented in Fig. 5, which shows hysteresis loops referring to the ferromagnetic nature of all samples. The $M(H)$ curves also show a linear part at higher magnetic fields signifying a meaningful paramagnetic contribution to the magnetization. The saturation magnetizations (M_s) are evaluated by extrapolating the plots of M vs. $1/H$ employing data at high magnetic fields [14]. The magnetic parameters are extracted from $M-H$ plots Fig.5 and listed in Table 3. The coercivity (H_c), remanent magnetization (M_r) are extracted from $M-H$ plots (Fig. 5) and listed with the saturation magnetizations (M_s) and the squareness values of the hysteresis loops for all specimens in Table 3. The small values of the coercivity (H_c) of CoFe₂O₄ nanoparticles denote that the studied samples lie near the superparamagnetic limit.

For the ideal inverse spinel crystal structure of CoFe₂O₄, with all the Co²⁺ ions located at the octahedral site, the magnetization per formula unit can be theoretically evaluated using Neel's two sub lattice model by considering the difference of total magnetic moments in octahedral and tetrahedral sites [15-18]

$M = M_{\text{octahedral}} - M_{\text{tetrahedral}}$. The magnetic moment of Fe³⁺ and Co²⁺ cations are 5.0 and 3.8 μ_B respectively, a theoretical magnetic moment of CoFe₂O₄ is 3.8 μ_B per formula unit. Based on the cation distribution obtained from XPS, the magnetization per formula units were also calculated and listed in Table 3, which shows that the magnetic moments changes with the preparation methods. The magnetic moment values of the investigated samples can be also determined experimentally by the following equation in Bohr magneton;

$$\mu_B = \text{Mol.wt} \times M_s / 5585 \quad (4)$$

However, the evaluated data from XPS and VSM are not equal, which can be associated to the finite size of nanoparticles conducting to the noncollinearity of magnetic moments on the surface of the nanoparticles. The disordered moments are developed due to the broken exchange bonds at the outer layer. On the other hand, the competition antiferromagnetic interactions precedes to a noncollinear arrangement of magnetic moments within interstitial sublattices which is induced because of the non-equilibrium cation distribution among tetrahedral and octahedral sites [15,17,18]. Shifting of larger Co²⁺ (0.78 Å) to substitute the smaller Fe³⁺ (0.645 Å) cations in octahedral sites produce strains on the surface due to the smaller space between the octahedral site cations comparable to the tetrahedral site cations in nanoparticles. The strains obtained can break the surface exchange bonds which cause the canted spin structure. This type of tetrahedral-octahedral interaction points to lower magnetization values in the ferrite nanoparticles compared with the bulk CoFe₂O₄ [17]. The low M_s -value of the investigate ferrite samples compared with that of the bulk one (80.9 emu/g) [3] can be also explained on the basis of the core-shell model, which clarifies that the finite-size effects of the nanoparticles manage to canting or non-collinearity of spins on their surface, in that way reducing magnetization [16].

To sum up, it can be said that the change in saturation magnetization with the variation in the preparation methods is possibly due to the rearrangement of the cation distribution, i.e., the exchange of Co^{2+} and Fe^{3+} ions from octahedral and tetrahedral sites and vice versa. The low values of M_s for the investigated samples could be credited to surface distortion which destabilizes the collinear spin arrangement and producing various canted spin structures at the surface. This effect is especially noticeable for ultrafine particles owing to their large surface to volume ratio. The reduction in coercivity with increasing particle size could be accredited from the combination of surface anisotropy and thermal energies [19].

The values of the squareness ratio (M_r/M_s) of investigated samples, shown in Table 3, are below 0.5 refers to that these samples are multidomain and the particles interact by magnetostatic interaction [20].

The magnetic anisotropy (K') has been also calculated using the following relation [21],

$$H_c = 0.98 K'/M_s \quad (5)$$

and the results obtained showed high values of 16711, 13571, and 6181 emu.Oeg^{-1} for CoFe_p , CoFe_g , and CoFe_s , respectively. The increase in K value is going parallel with increasing the presence of Co^{2+} ions in the octahedral sites, as shown in XPS results, Table 2.

The effect of the preparation method on the magnetic parameters of our CoFe_2O_4 nanoparticles is compared with other methods present in the literature and listed in Table 4.

3.3. Surface Properties

The surface properties of the spinels investigated were studied using the BET technique. The isothermal N_2 adsorption-desorption plots of these samples Fig.2S can be classified as type IV for CoFe_p and type V for CoFe_g and CoFe_s according to IUPAC, which is characteristic of the mesoporous material in which the adsorption proceeds via multilayer adsorption followed by capillary condensation. The hysteresis loops show the type H3 (aggregates of platelike particles forming slit-shaped pores) for all samples. The textural properties of the studied samples including BET-surface area, average pore diameter, pore-volume, and pore size distribution calculated from BJH method are derived from N_2 nitrogen adsorption/desorption isotherms and listed in Table 5. The data obtained refer to that the surface properties depend to a large extent on the method of preparation and CoFe_g exhibits the highest surface area.

3.4. Optical Properties

The prepared CoFe_2O_4 nanoparticles show still high magnetization, that photocatalyst appropriate for magnetically separable by a magnetic field and separation of photocatalyst from solution. Thus, the photocatalytic activity of the investigated samples has been studied. The optical absorption property related to the electronic structure characteristic is documented as the main factor in deciding the photocatalytic activity [30]. The diffuse reflectance spectra of our ferrites were recorded and converted to the Kubelka-Munk function, K-M, Fig. 6, using the following equation:

$$K-M = (1-R)^2 / 2R \quad (6)$$

Where R is absolute reflectance. The results obtained are listed in Fig. 6A. The spectra show that all synthesized CoFe_2O_4 samples exhibited photo-absorption in the visible light region, which implies the probability of high photocatalytic efficiency of these materials under visible light. The absorption behavior in the visible region is originated from the electronic charge transformation of Co^{2+} and Fe^{3+} to their conduction level in the conduction band [7, 31, 32]. The CoFe_2O_4 stoichiometry is organized in an incompletely inverse structure [27], with the Co^{2+} ion at both tetrahedral and octahedral sites, as shown in our results (XRD, XPS, and magnetic data). Broad Co–O and Fe–O charge transfers, together with d–d electron moves of Co^{2+} and Fe^{3+} in numerous coordination, guarantee the full absorption of the visible spectrum. The bandgap energies of the investigated ferrites were estimated according to Tauc's [33] by plotting $(KM \cdot h\nu)^{1/n}$ versus $h\nu$, where h is a Planck, s constant, ν is the light frequency and n is a constant relating to a mode of transition ($n = 1/2$ for allowed direct transition and $n = 2$ for indirect transition). Tauc's plots, shown in Fig.6-b, for every one of the specimens, demonstrated that the band-to-band direct transitions are more inclined to happen than the indirect transitions. The optical energy gaps, E_g , obtained from the intercept of the plot with the X-axis are recorded in Table 6, from which it can be seen that E_g value decreases with increasing the particle size and showed the smallest value for CoFe_g sample.

3.4.1. Raman Spectroscopy

Raman spectra were used to acquire vision on the vibrational energy states within the spinel ferrite obtained, as well as to review the structural characteristics and compositional regularity throughout the samples [34]. The spinel ferrite exhibit five active Raman vibration modes [35,36]. The Raman spectra of our samples showed only three bands, due to peak overlapping, at $284\text{-}297\text{ cm}^{-1}$, $460\text{-}470\text{ cm}^{-1}$, and $640\text{-}650\text{ cm}^{-1}$, as shown in Fig. 7, which was assigned as E_g , $3T_{2g}$ and $A_{1g}(1)$, respectively [37]. The $A_{1g}(1)$ band is related to symmetric stretching vibration mode at the tetrahedral (A) site. While $A_{1g}(1)$ band might be related to the vibration of Co-O bonds at the tetrahedral (A) site. The results obtained in Fig. 7; show that the frequency of Raman modes of the investigated spinels is slightly changed with the preparation method. This could be attributed to the variation in the cation distribution in the spinel lattice, as mentioned above.

3.4.2. Photoluminescence Study

Photoluminescence (PL) spectroscopy is an outstanding procedure to get valuable information concerning energy and the dynamics of charge carriers yielded during the exposure of light. The photoluminescence of the ferrite nanoparticles was studied using a 225 nm excitation wavelength source and the results obtained are presented in Fig. 8. The spectra of all samples show broad visible emission peaks at 434 - 442 nm, which are attributed to the charge transport between Co^{2+} at tetrahedral sites and Fe^{3+} at octahedral sites that are surrounded by O^{2-} ions [38]. The variation in the position and the intensity of luminescence can be explained on the basis that the PL-spectra are sensitive to the character of nanoparticles surface, due to the existence of gap surface disorders developing from surface non-stoichiometry and unsaturated bonds. The defects produced in the nanomaterial lattice during preparation are the base of luminescent properties [39]. The emission intensity of CoFe_g is lower than that of the rest samples. This indicates that this sample acted as

traps for the photo-induced charge carriers. These outcomes confirm the previously mentioned results on the influence of the preparation methods on the surface and optical properties.

3.4.3. Surface Acidity:

Temperature programmed desorption of ammonia (TPD-NH₃) is an appropriate procedure for measuring the quantity and the spreading of the acid sites on the surface of our samples. The acid site distribution results for the studied samples are summarized in Table 6. The ammonia desorbed at 100 °C contains some physisorbed ammonia as well as overstating the proportion of weak acid sites. Whereas, the ammonia desorbed at 220 – 370 °C and that at 450-600 °C are attributed to medium and strong acid sites, respectively [40]. The results obtained show that the acidity varies with preparation methods. For all samples, the strength of acidic sites follows the order: Weak acid sites > medium sites > strong acid sites. CoFe₉ exhibits the highest total acidity than that of other samples.

3.5. Photocatalytic Activity of CoFe₂O₄ Samples

According to the above-mentioned optical properties, we studied the photocatalytic activity of the investigated CoFe₂O₄ nanoparticles under visible light irradiation using the degradation of Basic Red 18 (BR 18) aqueous solution, as a basic dye model. Before the irradiation process, the suspended solution of the dye and catalyst was stored in the dark for 45 min. to assurance adsorption/desorption equilibrium. The photocatalytic degradation results are illustrated in Fig. 9. From which it can be seen that the degradation of the dye is very slow in the absence of the catalyst and the CoFe₉ sample showed the highest photocatalytic efficiency due to the high optical absorptions in vis. Light region with lower bandgap energy and a larger surface area. Therefore, this sample was selected to test the impact of catalyst dosage, dye concentration, and pH of the solution on the dye degradation rate. The results obtained given in Fig. 3S show that the rate of dye degradation has the highest rate at 3 mg/L catalyst dosage and decreases with increasing dye concentration in the range of 10 -100 ppm and has the highest rate at pH= 7 of the solution.

In view of literature reports, the kinetic of photocatalytic reaction can be calculated according to:

$$-\ln(C/C_0) = k_{obs} t \quad (7)$$

Where C₀ and C are the concentrations of dye at zero time and time t, respectively, and k_{obs} are the pseudo-first-order rate constant. The rate constant, k_{obs}, evaluated from the slope of the straight line of plotting -ln(C/C₀) vs. reaction time, Fig. 9-b showed a value of 0.1 min⁻¹.

3.5.1. Mechanism of Photocatalysis

The major oxidative species in the photocatalytic progression are positive holes (h⁺/VB) and the OH[•] hydroxyl radical formed during the irradiation process. In the present work, the trapping experiments were used to determine which one of these species is active for organic degradation. EDTA-2Na and isopropyl alcohol were used as an h⁺, and isopropyl alcohol as an OH[•] scavenger, respectively [32]. The results showed that the additive of isopropyl alcohol slightly changed the dye degradation indicating that OH[•] radicals were minor

factors in the photocatalytic degradation process, whereas the addition of h^+ capture (EDTA-2Na) caused a great decrease in the degradation efficiency as shown in Fig. 10. This foundation distinctly denoted that positive holes are the major active species of the dye dissociation.

Conclusions

Nanosized cobalt ferrite (CoFe_2O_4) particles are synthesized through three different methods (sol-gel, solid-state blending, and co-precipitation). The proposed preparations are inexpensive and thus appropriate for the large-scale production of such type nanoparticles. XRD approves the formation of a spinel phase in all preparation methods. The FT-IR spectra displayed two characteristic metal-oxygen, vibrational bands for the spinel structure. The results reveal that the synthetic route affected each of the particle size, morphological structure, surface textures, surface acidic properties, cation distribution, optical and magnetic properties. Both Fe^{3+} and Co^{2+} are distributed in octahedral and tetrahedral sites in a ratio depending on the preparation method. The variation in this ratio controlled the studied properties. The results showed that the prepared ferrite exhibits either ferromagnetic or super-paramagnetic behavior with magnetic parameters of particular importance for allowing the magnetic recovery and reuse of the catalyst and the possibility to be used in recording media. Ammonia TPD analyses showed that weak acid sites prevail medium-strength sites, whereas the number of strong acid sites is the least. The obtained ferrite is utilized as photocatalytic for degradation Basic Red 18 (BR 18) dye under visible light irradiation with the highest degradation rate for the sample prepared by the gel method. The prepared ferrite photocatalysts can potentially be used for cleaning polluted water with the help of magnetic separation.

References

1. D. Carta, M. F. Casula, A. Falqui, D. Loche, G. Mountjoy, C. Sangregorio, A. Corrias, A Structural and Magnetic Investigation of the Inversion Degree in Ferrite Nanocrystals MFe_2O_4 (M = Mn, Co, Ni), *J. Phys. Chem. C* 113(20) (2009) 8606-8615.
2. T. Prabhakaran, R.V. Mangalaraja, J.C. Denardin, J.A. Jimenez, The effect of calcination temperature on the structural and magnetic properties of co-precipitated CoFe_2O_4 nanoparticles. *J. Alloys Compd.* 716 (2017) 171–183.
3. R. Safi, A. Ghasemi, R. Shoja-Razavi, Factors controlling magnetic properties of CoFe_2O_4 nanoparticles synthesized by chemical co-precipitation: Modeling and optimization using response surface methodology. *Ceram. Int.* 42 (2016) 15818–15825.
4. B. Vilém, S. David, H. Štěpán, M. Švecová, U. Pavel, J. Ondrej, Synthesis and Properties of Nanosized Stoichiometric Cobalt Ferrite Spinel, *Materials* 11(2018) 1241.
5. M. Jalalian, S.M. Mirkazemi, S. Alamolhoda, Phase constituents and magnetic properties of the CoFe_2O_4 nanoparticles prepared by polyvinylpyrrolidone (PVP)-assisted hydrothermal route. *Appl. Phys. A* 122 (2016) 835.
6. M. Liu, M. Lu, L. Wang, S.C. Xu, J.L. Zhao, Li, H.B. Mossbauer study on the magnetic properties and cation distribution of CoFe_2O_4 nanoparticles synthesized by hydrothermal method. *J. Mater. Sci.* 51 (2016) 5487–5492.

7. R.S. Yadav, J. Havlica, J. Masilko, L. Kalina, M. Hajduchova, V. Enev, J. Wasserbauer, I. Kuritka, Z. Kozakova, Structural, cation distribution, and magnetic properties of CoFe_2O_4 spinel ferrite nanoparticles synthesized using a starch-assisted sol-gel auto-combustion method. *J. Supercond. Nov. Magn.* 28 (2015) 1851–1861.
8. M. Khairy, M.A. Mousa, Influences of γ -Radiation and Surfactants on Electrical and Magnetic Properties of $\text{Cu}_{0.1}\text{Zn}_{0.9}\text{Mn}_2\text{O}_4$ Nanoparticles, *Intern. J. Mater. Chem.* 2(5) (2012) 197-204.
9. Y. Koseoglu, F. Alan, M. Tan, R. Yilgin, Ozturk, M. Low temperature hydrothermal synthesis and characterization of Mn doped cobalt ferrite nanoparticles. *Ceram. Inter.* 38(5) (2012) 3625 -3634.
10. P.P. Hankare, V.T. Vader, N.M. Patil, S.D. Jadhav, U.B. Sankpal, M.R. Kadam, B.K. Chougule, N.S. Gajbhiye, Synthesis, characterization and studies on magnetic and electrical properties of Mg ferrite with Cr substitution. *J. Mater. Chem. Phys.* 113(1) (2009) 233-238.
11. N.W. Grimes, On the specific heat of compounds with spinel structure - II. Zinc ferrite, a paramagnetic compound with magnetic ion occupying the octahedral site. *Proc. R. Soc. Lond. A*, 338(1) (1974) 223-233.
12. F.D. Monte, M.P. Morales, D. Levy, A. Fernandez, M. Ocaña, A. Roig, E.; O'Grady, K. Molins, C.J. Serna, Formation of $\gamma\text{-Fe}_2\text{O}_3$ Isolated Nanoparticles in a Silica Matrix. *Langmuir.* 13(14) (1997) 3627-3634.
13. S.X. Zhang, H.Y. Niu, Y.Q. Cai, X.L. Zhao, Y.L. Shi, Arsenite and Arsenate adsorption on coprecipitated bimetal oxide magnetic nanomaterials: MnFe_2O_4 and CoFe_2O_4 . *J. Chem. Eng.* 158(3) (2010) 599-607.
14. V.P. Annie, N.M.G. Immaculate, K. Mahalakshmi, M. L. Ansel, D.S. Jerome, Study on Cobalt Ferrite Nanoparticles Synthesized by Co-Precipitation Technique for Photo-Fenton Application. *Mech. Mater. Sci. Eng.* 9(1) (2017) 110-115.
15. J. Jacob, M.A. Khadar, Investigation of mixed spinel structure of nanostructured nickel ferrite. *J. Appl. Phys.* 107 (2010) 114310.
16. R.H. Kodama, A.E. Berkowitz, Surface Spin Disorder in NiFe_2O_4 Nanoparticles. *J. Phys. Rev. Lett.* 77(2) (1996) 394-397.
17. Y. Zhang, Y. Liu, C. Fei, Z. Yang, L. Zhihong, R. Xiong, D. Yin, J. Shi, The temperature dependence of magnetic properties for cobalt ferrite nanoparticles by the hydrothermal method. *J. Appl. Phys.* 108 (2010) 084312.
18. C. Vazquez-Vazquez, M.A. Lopez-Quintela, M.C. Bujan-Nunez, J. Rivas, Finite Size and Surface Effects on the Magnetic Properties of Cobalt Ferrite Nanoparticles. *J. Nanopart. Res.* 13(4) (2011) 1663-1676.
19. K. Maaz, A. Mumatz, S. K. Hasanain, A. Ceylan, Synthesis and Magnetic Properties of Cobalt Ferrite (CoFe_2O_4) Nanoparticles Prepared by Wet Chemical Route. *J. Magn. Magn. Mater.* 308(2) (2007) 289-295.
20. A.C. Druc, A.M. Dumitrescu, A.I. Borhan, V. Nica, A.R. Iordan, M.N. Palamaru, Optimization of synthesis conditions and the study of magnetic and dielectric properties for MgFe_2O_4 ferrite. *Cent. Eur. J. Chem.* 11(8) (2013) 1330-1342.
21. E.E. Ateia¹, G. Abdelatif, F.S. Soliman, Optimizing the physical properties of calcium nano ferrites to be suitable in many applications, *J Mater. Sci. Mater. Elect.* 28 (2017) 5846–5851.

22. A. Mazrouei, A. Saidi, Microstructure and magnetic properties of cobalt ferrite nano powder prepared by solution combustion synthesis, *J. Mater. Chem. Phys.* 209 (2018) 152-158.
23. B. Purnama , A.T. Wijayanta, Suharyana, Effect of calcination temperature on structural and magnetic properties in cobalt ferrite nano particles, *J. King Saud Univ. Sci.*31(4) (2019) 956-960.
24. K..S. Rao, GSVRK.Choudaryb, K.H.Rao, Ch.Sujatha, Structural and Magnetic properties of Ultrafine CoFe_2O_4 , *J. Nanoparticles. J. Proc. Mater. Sci.* 10(2015) 19-27.
25. M. Kurian, S. Thankachan, D. S. Nair, E. K . Aswathy. A. Babu, A. Thomas , B. Krishna K. T. J. *Adv. Ceram.*4 (2015) 199-205.
26. D. Kovacheva, T. Ruskov, P. Krystev, S. Asenov, N. Tanev, I. Mönch, R. Koseva,U. Wolff, T. Gemming, M. Markova-Velichkova, D. Nihtianova, K.-F. Arndt, Synthesis and characterization of magnetic nano-sized Fe_3O_4 and CoFe_2O_4 , *J. Bulg. Chem. Commun.* , 44(2012) 90-97. Proceedings of the IIIrd National Crystallographic Symposium.
27. T. George, A. T. Sunny, T. Varghese, Magnetic properties of cobalt ferrite nanoparticles synthesized by sol-gel method. *Mater. Sci. and Eng.* 73 (2015) 012050. Doi:10.1088/1757-899X/73/1/012050
28. M. P. Reddy, A.M.A.Mohamed, X.B.Zhou, S.Duc, Q.Huang, A facile hydrothermal synthesis, characterization and magnetic properties of mesoporous CoFe_2O_4 nanospheres , *J Magn. Magnet. Mater.* 388(2015) 40-44.
29. N.R. Panchal, R.B. Jotania, Cobalt ferrite nano particles by microemulsion route *J. Nanotech. Nanosci.* 1(1) (2010) 17-18.
30. P. Sathishkumar, R.V. Mangalaraja, S. Anandan, M. Ashokkumar, $\text{CoFe}_2\text{O}_4/\text{TiO}_2$ nanocatalysts for the photocatalytic degradation of Reactive Red 120 in aqueous solutions in the presence and absence of electron acceptors. *J. Chem. Eng.* 220 (2013) 302–310.
31. Y. Koseoglu, F. Alan, M.; Tan, R. Yilgin, M. Ozturk, Low temperature hydrothermal synthesis and characterization of Mn doped cobalt ferrite nanoparticles. *J. Ceram. Inter.* 38(5) (2012) 3625-3634.
32. M. Lenglet, F. Hochu, J. Durr, Optical Properties of Mixed Cobalt Ferrites. *J. Phys. IV, C1/7* (1997) 259-260.
33. J. Tauc, *Amorphous and liquid semiconductor* (New York: Plenum) (1974) 159.
34. B. Schrader, *Infrared and Raman Spectroscopy: Methods and Applications*, VCH: Weinheim, Germany, 100(7) (1995) 807.
35. R. Nongjai, S. Khan, K. Asokan, H. Ahmed, I. Khan, Magnetic and electrical properties of In doped cobalt ferrite nanoparticles. *J. Appl. Phys.* 112 (2012) 084321.
36. S. Thota, S.C. Kashyap, S.K. Sharma, V.R. Reddy, Cation distribution in Ni-substituted $\text{Mn}_{0.5}\text{Zn}_{0.5}\text{Fe}_2\text{O}_4$ nanoparticles: A Ramman, Mossbauer, X-ray diffraction and electron spectroscopy study. *Mater. Sci. Eng. B* , 206 (2016) 69-78.
37. S. Ayyappan, S. Mahadevan, P. Chandramohan, M.P. Srinivasan, J. Philip, B. Raj, Influence of Co^{2+} ion concentration on the size, magnetic properties and purity of CoFe_2O_4 spinel ferrite nanoparticles. *J. Phys. Chem. C.* 114(14) (2010) 6334-6341.
38. R.B. Kale, C.D. Lokhande, Influence of air annealing on the structural, optical and electrical properties of chemically deposited CdSe nano-crystallites. *Appl. Surf. Sci.* 223(4) (2004) 343-351.

39. Y. Lin, J. Zhang, E.H. Sargent, E. Kumacheva, Photonic pseudo-gap-based modification of photoluminescence from CdS nanocrystal satellites around polymer microspheres in a photonic crystal . Appl. Phys. Lett. 81 (2002) 3134.
40. C.G. Ramankutty, S. Sugunan, B. Thomas, Study of cyclohexanol decomposition reaction over the ferrosinels $A_{1-x}Cu_xFe_2O_4$ (A = Ni or Co and x = 0, 0.3, 0.5, 0.7 and 1) prepared by 'soft' chemical methods. J. Mol. Catal. A: Chem. 187(2002)105–117.

Tables

Table 1. Lattice constant, density, particle Size values and FT-IR data of the studied $CoFe_2O_4$ samples.

Sample	Lattice constant(Å)	X-ray density (g/cm ³)	XRD-particle size (nm)	TEM-Particle size (nm)	Tetrahedral vibration n_1 (cm ⁻¹)	Octahedral Vibration n_2 (cm ⁻¹)	OH-group	δ H-O-H bonding
CoFe _g	8.387	5.282	21	23	563	402	3428	1640
CoFe _p	8.392	5.267	31	28	579	413	3432	1625
CoFe _s	8.412	5.235	36	39	581	428	3439	1635

Table 2. XPS results of the investigated $CoFe_2O_4$ samples.

Sample	Spectrum	BE(eV)	Assignment	atomic %	Particle Size (nm)
CoFe _s	Co 2p ^{3/2}	780.3	Octahedral Co ²⁺	48	36
		782.1	tetrahedral Co ²⁺	52	
		785	satellite peak of Co ²⁺	-	
	Fe 2p ^{3/2}	711	octahedral Fe ³⁺	76	
		713.5	tetrahedral Fe ³⁺	24	
		717	Satellite peak Fe ³⁺	-	
O 1s	529.85	CoFe ₂ O	73		
	531.5	CoFe ₂ O ₄	16		
	534	Artifact	11		
CoFe _p	Co 2p ^{3/2}	780	Octahedral Co ²⁺	55	31
		781.9	tetrahedral Co ²⁺	45	
		785.5	satellite peak of Co ²⁺	-	
	Fe 2p ^{3/2}	710.5	octahedral Fe ³⁺	72.5	
		713.2	tetrahedral Fe ³⁺	27.5	
		716.7	Satellite peak Fe ³⁺	-	
	O 1s	529.7	CoFe ₂ O ₄	80	
		531.5	CoFe ₂ O ₄	12	
		534.5	Artifact	8	
CoFe _g	Co 2p ^{3/2}	779.9	Octahedral Co ²⁺	63	21
		781.6	tetrahedral Co ²⁺	37	
		784.4	Octahedral Co ²⁺	-	
	Fe 2p ^{3/2}	710.9	octahedral Fe ³⁺	68.5	
		713.1	tetrahedral Fe ³⁺	31.5	
		717.1	Satellite peak Fe ³⁺	-	
	O 1s	529.9	CoFe ₂ O ₄	78	
		531.5	CoFe ₂ O ₄	13	

Table 3. Particle Size, Magnetic parameters and cation distribution of CoFe₂O₄ Samples.

Sample	D _{xrd} (nmr)	M _s (emu/g)	M _r (emu/g)	H _c (Oe)	M _r /M _s	m _B (exp.)	m _B (theory)	Cation distribution
Bulk	—	80.8	—	—	—	—	3.8	(Co)[Fe ₂]O
CoFe _g	21	38.0	10.1	370	0.27	1.60	4.7	(Co _{0.37} Fe _{0.63})
CoFe _p	31	43.1	12.5	360	0.29	1.81	4.88	[Co _{0.63} Fe _{1.37}]O ₄
CoFe _s	36	46.6	3.69	130	0.08	1.96	5.04	(Co _{0.45} Fe _{0.55}) [Co _{0.55} Fe _{1.45}]O ₄ (Co _{0.52} Fe _{0.48}) [Co _{0.48} Fe _{1.52}]O ₄

Table 4. Effect of the preparation methods on magnetic parameters of CoFe₂O₄ nanoparticles

<i>Preparation method</i>	<i>Particle Size (nm)</i>	<i>M_s (emu/g)</i>	<i>M_r (emu/g)</i>	<i>H_c (Oe)</i>	<i>Reference</i>
Green	21	38.0	10.1	370	Present work
Co-precipitation	31	43.1	12.5	360	Present work
ceramic	36	46.6	3.69	130	Present work
copmbustion	33	31.6	9.6	870	[22]
Co-precipitation	32	35.6	13	614	[23]
Sol-gel	5.5	42.4	8.9	434	[24]
Co-precipitation	42	27	8.7	500	[25]
Co-precipitation	21	10.4	10	30	[26]
Sol-gel	18	30	10	100	[27]
hydrothermal	120	60	23	150	[28]
Microemulsion	28	1.58	0.612	1357	[29]

Table 5. Textural surface data obtained from BET measurements for CoFe₂O₄ Samples.

Samples	Particle size d_{XRD} (nm)	V_{st} (ml/g)	V_p (ml/g)	V_m (ml/g)	S_{BET} (m ² /gm)	r (Å)
CoFe _s	36	62	0.09	6	25	98
CoFe _p	31	138	0.21	10	45	89
CoFe _g	21	261	0.40	32	99	73

Table 6. Optical and surface acidity data of CoFe₂O₄ samples.

Samples	Particle size (nm)	λ_{max} (nm)	E_g (eV)	Surface Acidity sites	Surface Acidity sites medium (mmol/g)	Surface Acidity sites	Surface Acidity
				Weak (mmol/g)		Strong (mmol/g)	Total sites (mmol/g)
Bulk	—	790	2.0	-	-	-	-
CoFe _s	36	590	1.39	7.5	5.5	3.0	16.0
CoFe _p	31	610	1.38	6.0	4.1	2.1	13.2
CoFe _g	21	620	1.37	11.0	6.1	4.0	21.1

Figures

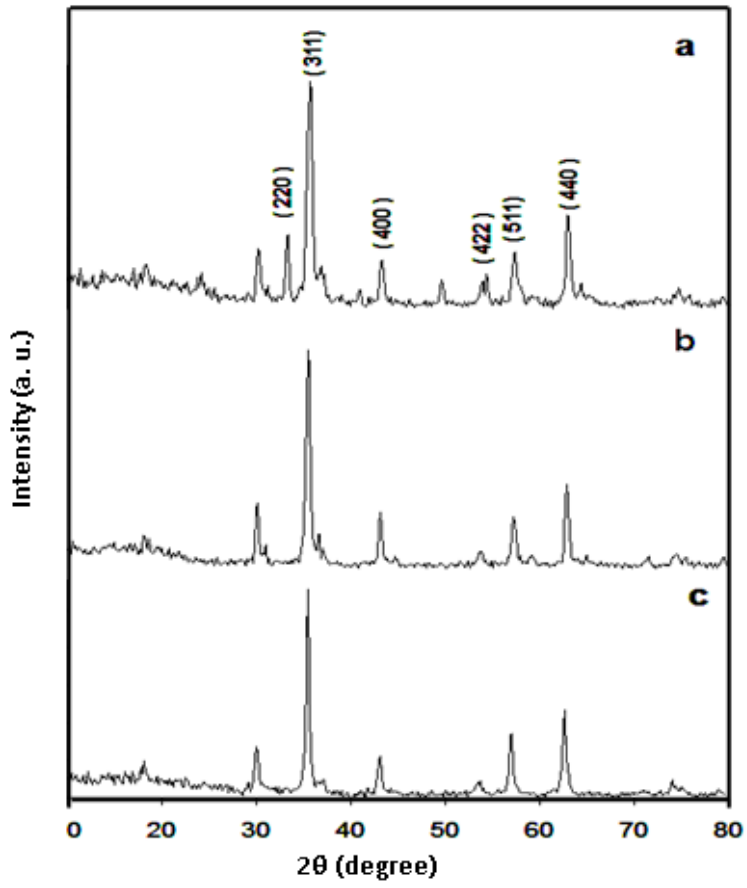


Figure 1

XRD patterns of the prepared CoFe₂O₄ ferrites are shown in Fig.1.

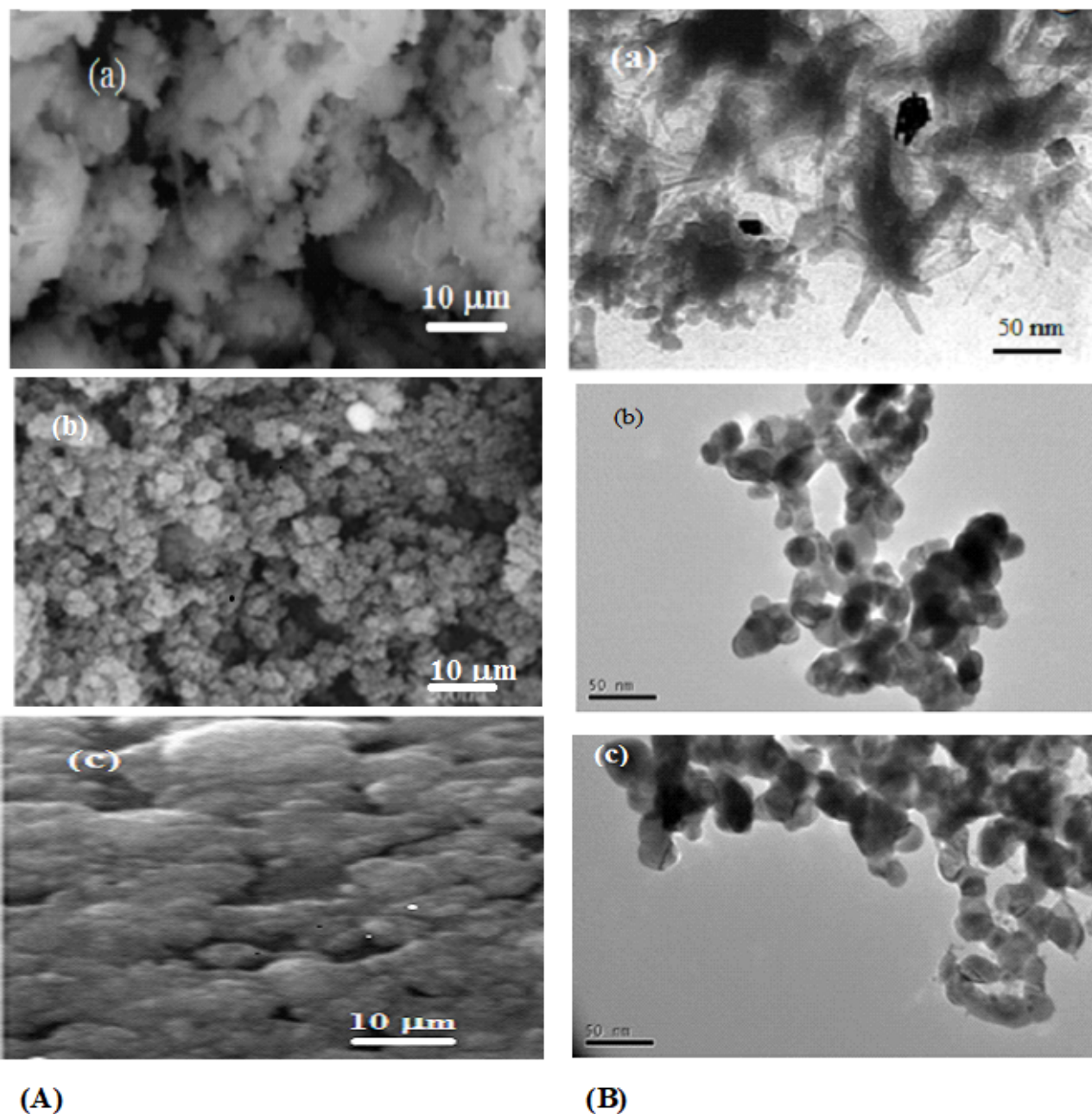


Figure 2

The SEM and TEM micrographs of the as-synthesized CoFe_2O_4 particles are given in Figs.2 (a and b). As seen, depending on the preparation method the nano-particles have been developed in different orders and clusters. SEM and TEM images of CoFe_2O_4 show morphology nanoparticles predominated by nanorods structure. The other cobalt ferrite specimens, CoFe_2O_4 and CoFe_2O_4 , demonstrates aggregated spherical particles besides particles with polygon morphologies. The variation in the morphology of the NPS shown in Figure 2.b denotes that the crystal growth of CoFe_2O_4 depends to a large extent on the preparation method. The nanoparticle sizes were obtained using histograms of 100 particles observed in the TEM image are listed in Table 1. The slight contrast found in the results of XRD and TEM is due to the different handles of the two tools. TEM analysis offers a number-average size distribution, XRD manifests a volume -averaged median size. In XRD, the correctness of Scherrer's formula is influenced by numerous variables, for example,

diffraction line width, and surface tension. Thus, Scherrer's equation might cause particular errors in determining the fixed value of the crystallite size [7].

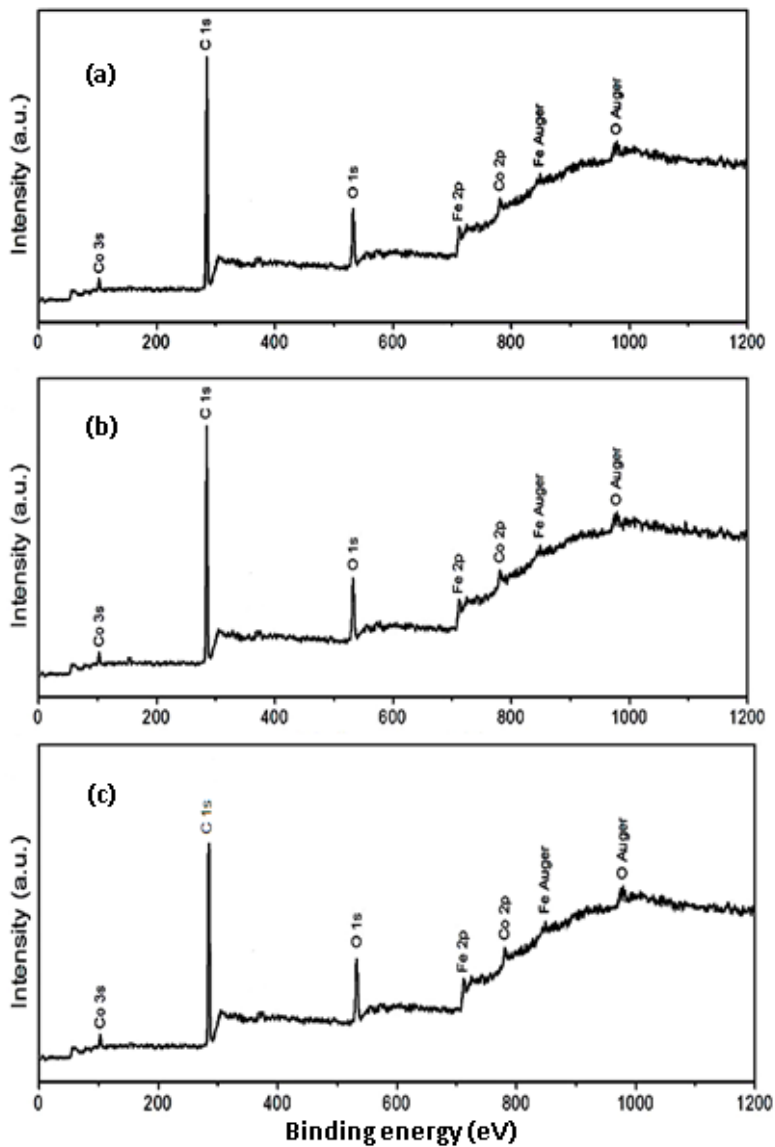


Figure 3

XPS results of the CoFe₂O₄ samples are given in Fig. 3, where binding energy (B.E.) ranges from 0 to 1200 eV. The spectra show that the samples contain only the main elements: Fe, Co, and O beside the contaminated C element coming from the environment. The binding energy (B.E.) values obtained attached well with the literature data for CoFe₂O₄, Table 2, [13] proving that pure ferrite had been produced.

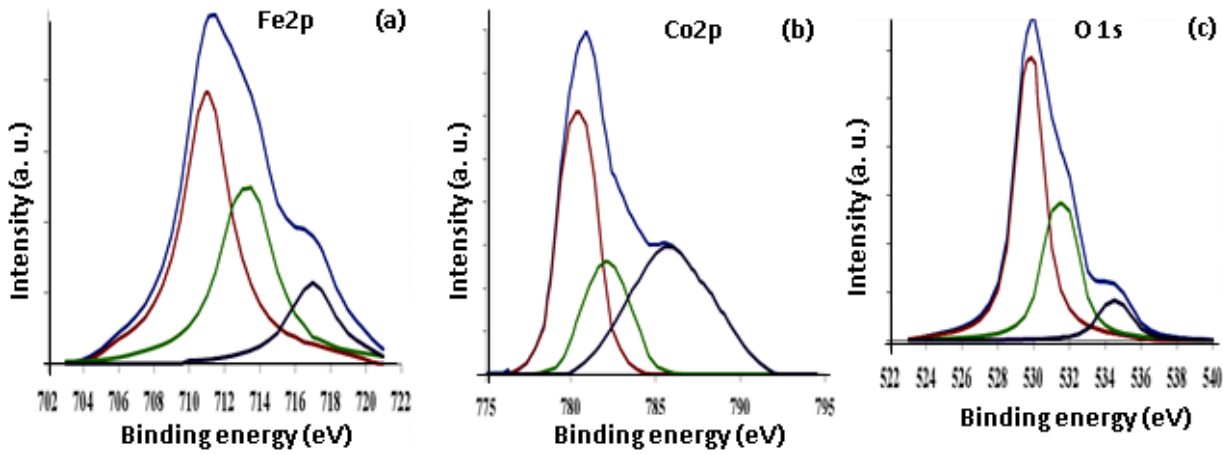


Figure 4

To investigate the cation valence states and their distribution in the CoFe_2O_4 spinel, the high-resolution XPS spectra of Fe 2p, Co 2p, and O 1s peaks of the CoFe_2O_4 specimen were studied and given for CoFe_2O_4 in Fig. 4. The integrated intensities of the fitted peaks of Co^{2+} and Fe^{3+} ions were used to determine their distributions in both octahedral and tetrahedral positions. The table also shows an increase in the concentration of Fe^{3+} cations on octahedral sites with the increase in the particle size of the sample, which agrees well with XRD data. In conclusion, it can be said that the selection of the preparation route is effective in controlling the cation distribution within the spinel lattice. The presence of high intense satellite structure on the high binding energy side of the Co 2p_{3/2} and Fe 2p_{3/2} might be attributed to the band structure related to octahedral Co 2p in the oxide lattice.

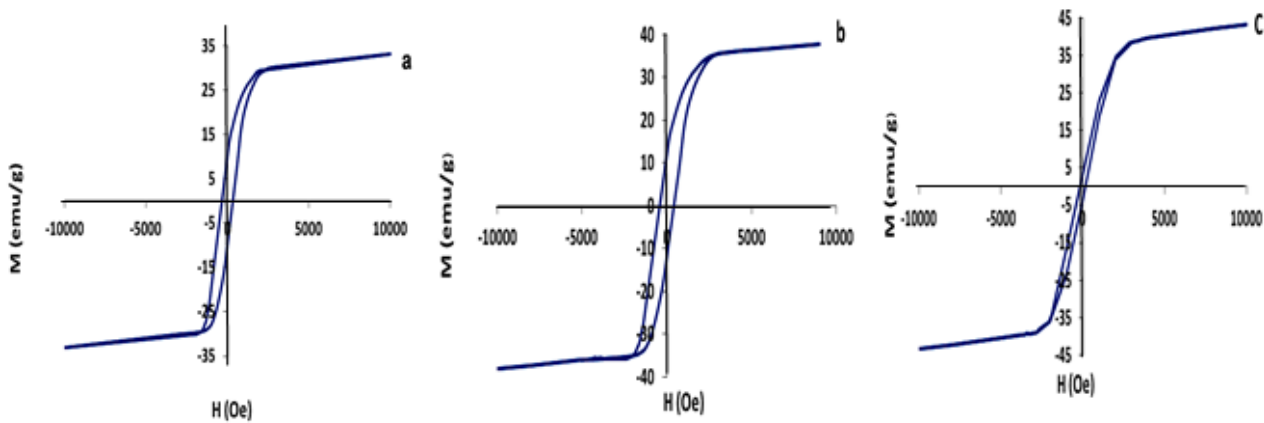


Figure 5

In order to investigate the effect of synthetic method on the magnetic properties, the VSM test was done at room temperature in an applied field of 10 kOe. The results are represented in Fig. 5, which shows hysteresis loops referring to the ferromagnetic nature of all samples. The $M(H)$ curves also show a linear part at higher magnetic fields signifying a meaningful paramagnetic contribution to the magnetization. The saturation magnetizations (M_s) are evaluated by extrapolating the plots of M vs. $1/H$ employing data at high magnetic fields [14]. The magnetic parameters are extracted from $M-H$ plots Fig.5 and listed in Table 3. The coercivity (H_c), remanent magnetization (M_r) are extracted from $M-H$ plots (Fig. 5) and listed with the saturation

magnetizations (Ms) and the squareness values of the hysteresis loops for all specimens in Table 3. The small values of the coercivity (Hc) of CoFe₂O₄ nanoparticles denote that the studied samples lie near the superparamagnetic limit.

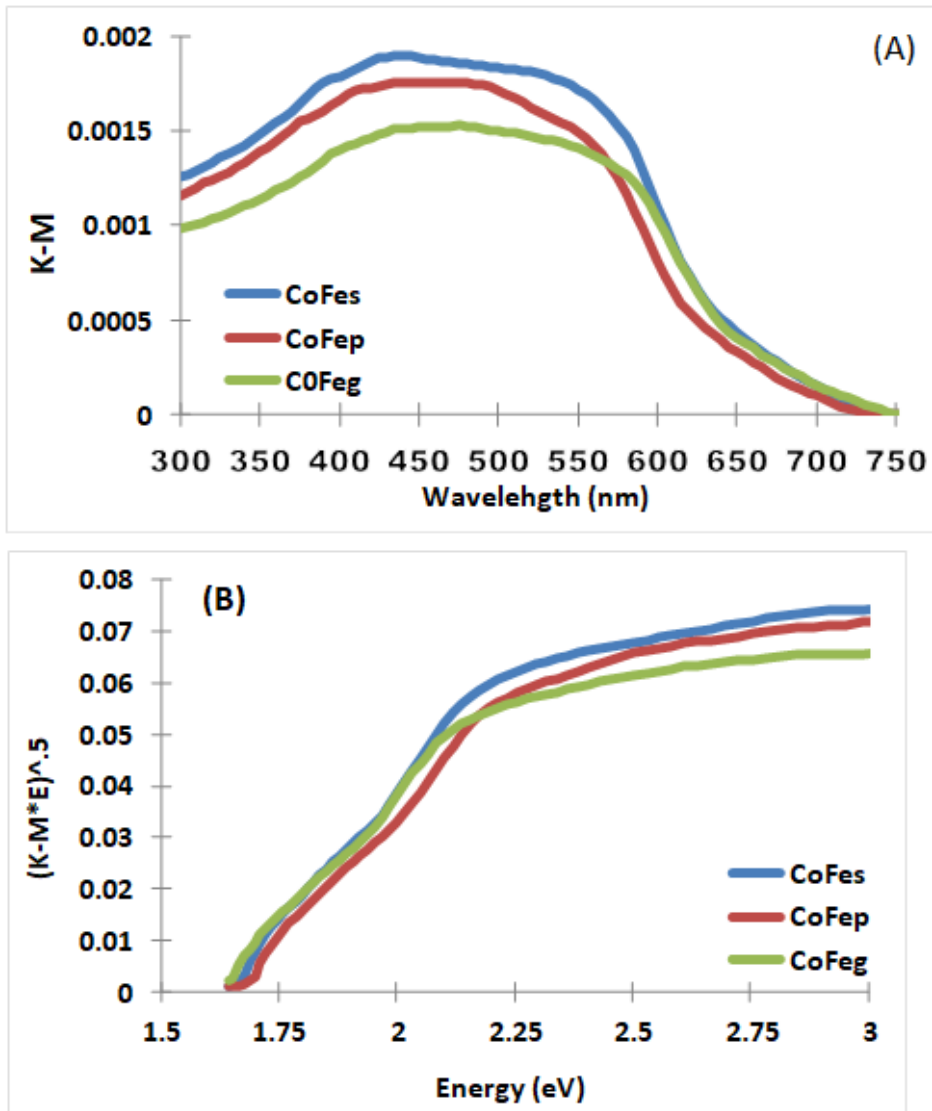


Figure 6

Where R is absolute reflectance. The results obtained are listed in Fig. 6A. The spectra show that all synthesized CoFe₂O₄ samples exhibited photo-absorption in the visible light region, which implies the probability of high photocatalytic efficiency of these materials under visible light. The absorption behavior in the visible region is originated from the electronic charge transformation of Co²⁺ and Fe³⁺ to their conduction level in the conduction band [7, 31, 32]. The CoFe₂O₄ stoichiometry is organized in an incompletely inverse structure [27], with the Co²⁺ ion at both tetrahedral and octahedral sites, as shown in our results (XRD, XPS, and magnetic data). Broad Co–O and Fe–O charge transfers, together with d–d electron moves of Co²⁺ and Fe³⁺ in numerous coordination, guarantee the full absorption of the visible spectrum. The bandgap energies of the investigated ferrites were estimated according to Tauc's [33] by plotting $(KM \cdot h\nu)^{1/n}$ versus $h\nu$, where h is a Planck constant, ν is the light frequency and n is a constant relating to a mode of transition ($n = 1/2$ for allowed direct transition and $n = 2$ for indirect transition). Tauc's plots, shown in Fig.6-b,

for every one of the specimens, demonstrated that the band-to-band direct transitions are more inclined to happen than the indirect transitions. The optical energy gaps, E_g , obtained from the intercept of the plot with the X-axis are recorded in Table 6, from which it can be seen that E_g value decreases with increasing the particle size and showed the smallest value for CoFeg sample.

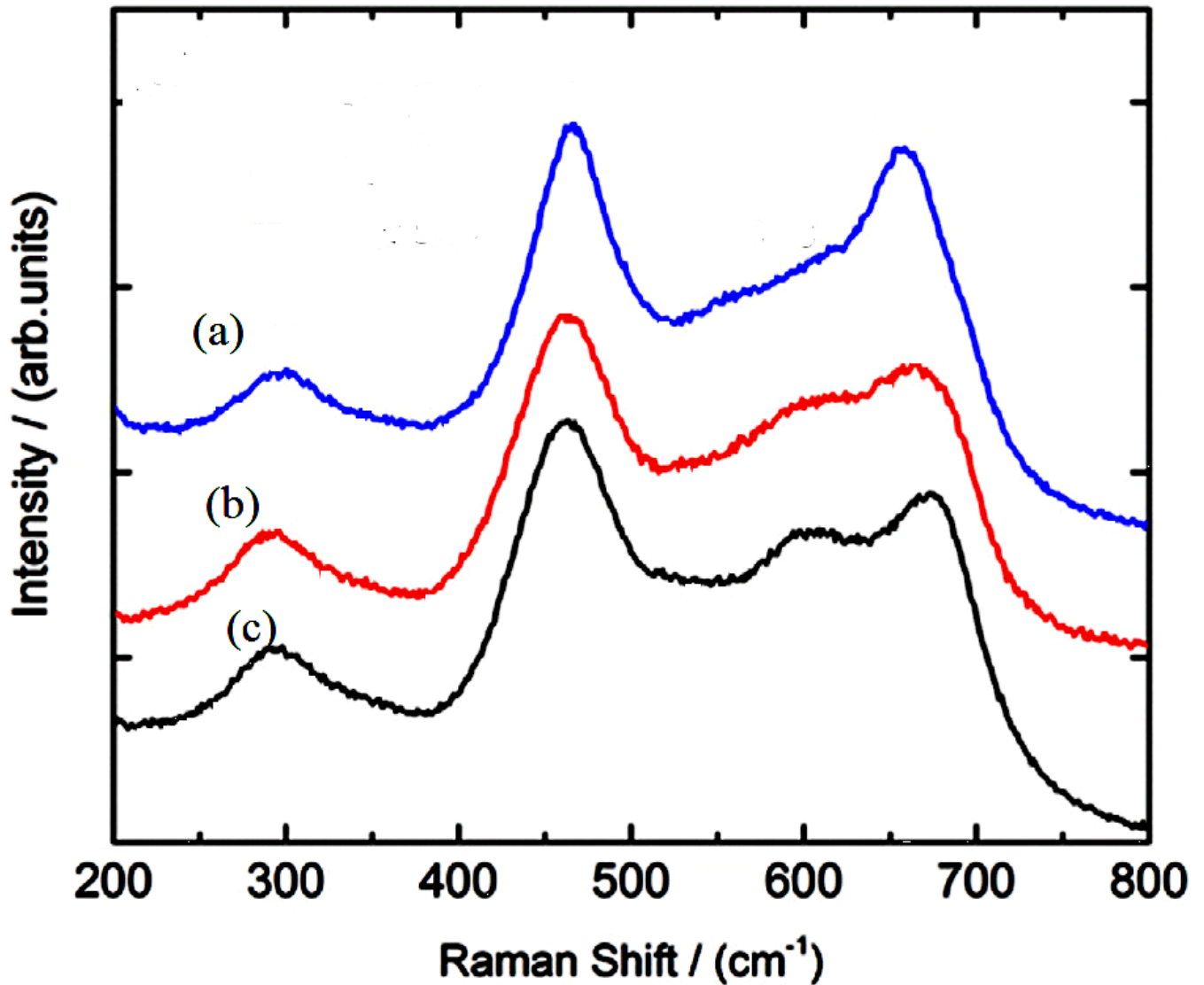


Figure 7

Raman spectra were used to acquire vision on the vibrational energy states within the spinel ferrite obtained, as well as to review the structural characteristics and compositional regularity throughout the samples [34]. The spinel ferrite exhibit five active Raman vibration modes [35,36]. The Raman spectra of our samples showed only three bands, due to peak overlapping, at 284-297 cm⁻¹, 460-470 cm⁻¹, and 640-650 cm⁻¹, as shown in Fig. 7, which was assigned as E_g , $3T_{2g}$ and $A_{1g}(1)$, respectively [37]. The $A_{1g}(1)$ band is related to symmetric stretching vibration mode at the tetrahedral (A) site. While $A_{1g}(1)$ band might be related to the vibration of Co-O bonds at the tetrahedral (A) site. The results obtained in Fig. 7; show that the frequency of Raman modes of the investigated spinels is slightly changed with the preparation method. This could be attributed to the variation in the cation distribution in the spinel lattice, as mentioned above.

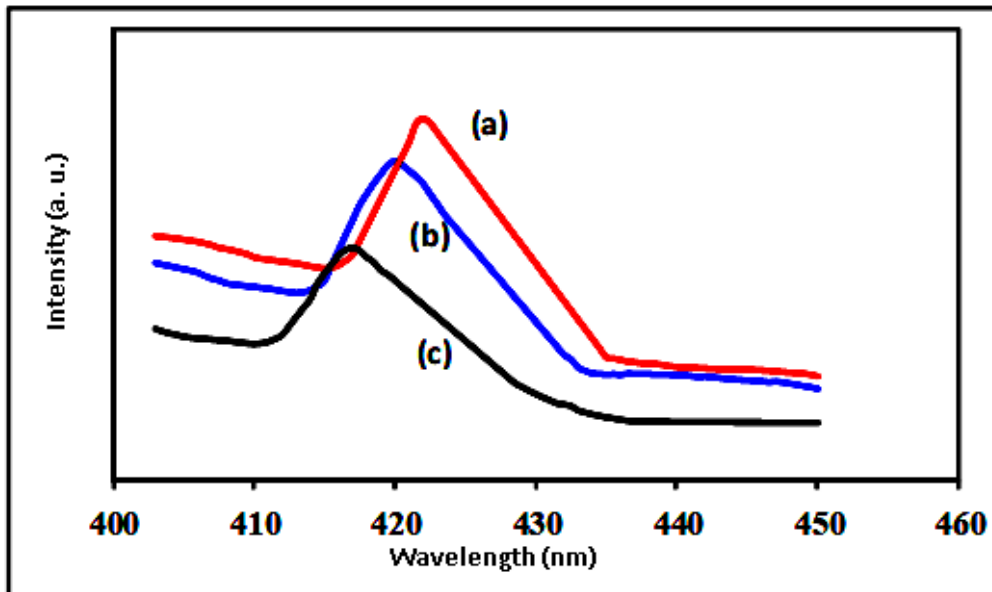


Figure 8

Photoluminescence (PL) spectroscopy is an outstanding procedure to get valuable information concerning energy and the dynamics of charge carriers yielded during the exposure of light. The photoluminescence of the ferrite nanoparticles was studied using a 225 nm excitation wavelength source and the results obtained are presented in Fig. 8. The spectra of all samples show broad visible emission peaks at 434 - 442 nm, which are attributed to the charge transport between Co^{2+} at tetrahedral sites and Fe^{3+} at octahedral sites that are surrounded by O_2^- ions [38]. The variation in the position and the intensity of luminescence can be explained on the basis that the PL-spectra are sensitive to the character of nanoparticles surface, due to the existence of gap surface disorders developing from surface non-stoichiometry and unsaturated bonds. The defects produced in the nanomaterial lattice during preparation are the base of luminescent properties [39]. The emission intensity of CoFeg is lower than that of the rest samples. This indicates that this sample acted as traps for the photo-induced charge carriers. These outcomes confirm the previously mentioned results on the influence of the preparation methods on the surface and optical properties.

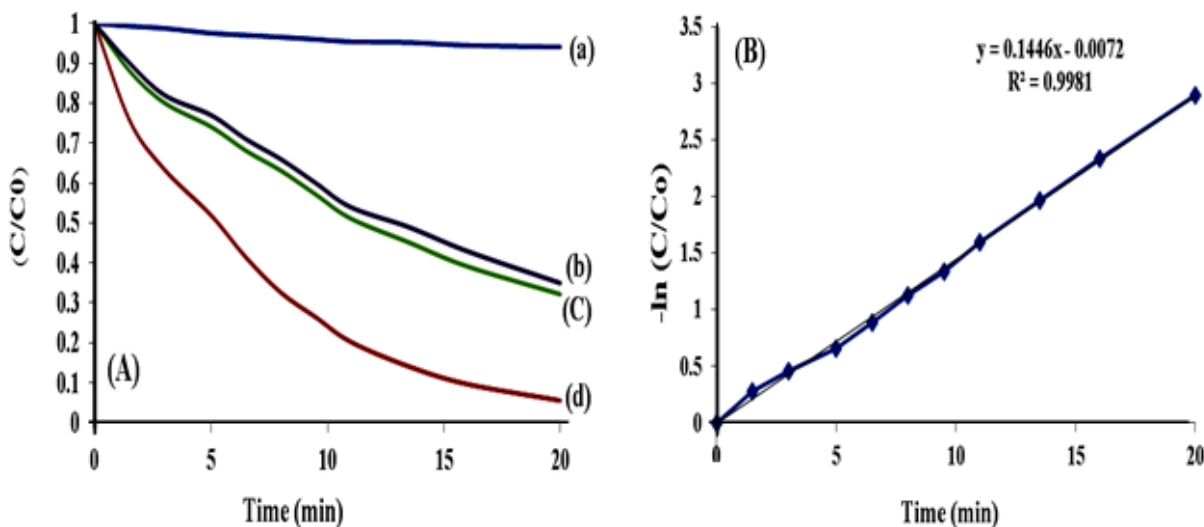


Figure 9

Basic Red 18 (BR 18) aqueous solution, as a basic dye model. Before the irradiation process, the suspended solution of the dye and catalyst was stored in the dark for 45 min. to assurance adsorption/desorption equilibrium. The photocatalytic degradation results are illustrated in Fig. 9.

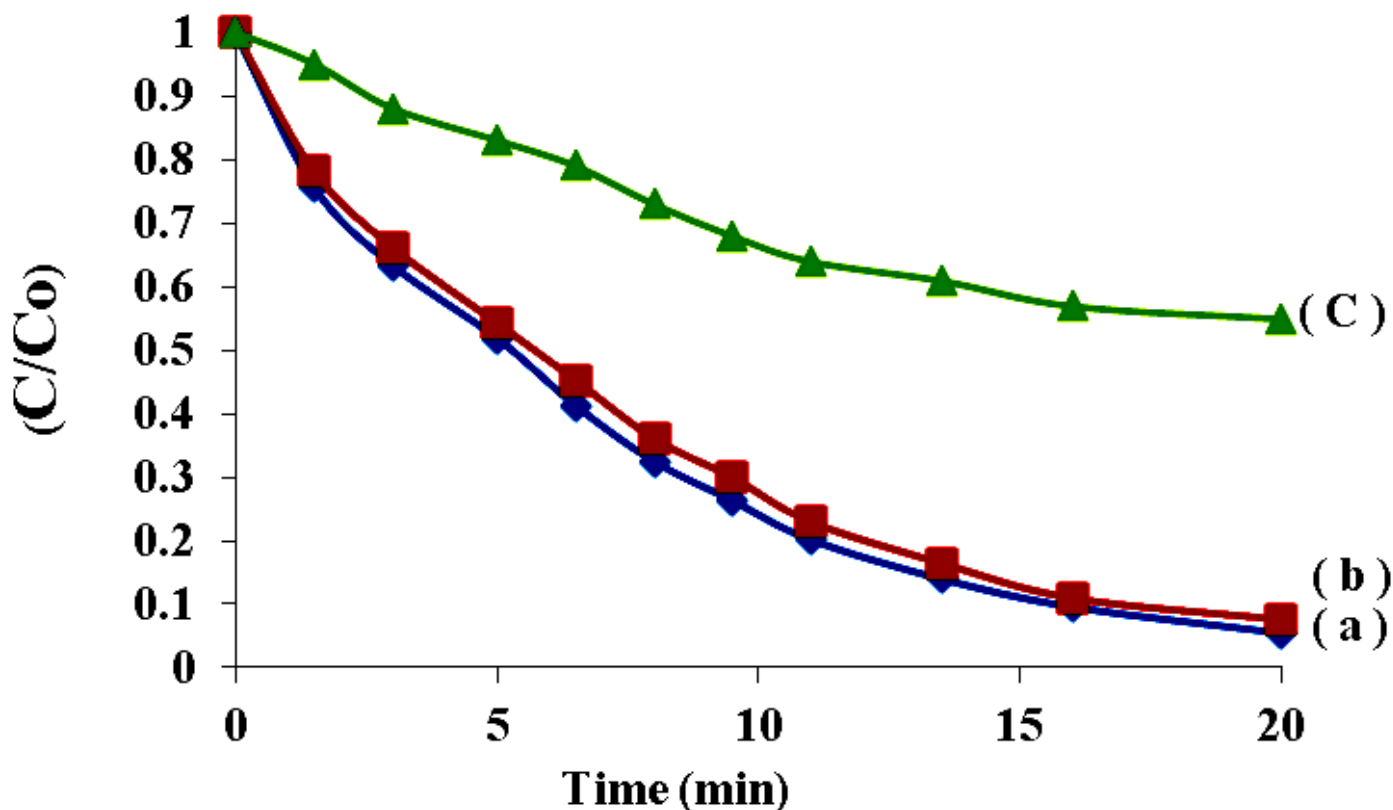


Figure 10

The major oxidative species in the photocatalytic progression are positive holes (h^+/VB) and the $OH\cdot$ hydroxyl radical formed during the irradiation process. In the present work, the trapping experiments were used to determine which one of these species is active for organic degradation. EDTA-2Na and isopropyl alcohol were used as an h^+ , and isopropyl alcohol as an $OH\cdot$ scavenger, respectively [32]. The results showed that the additive of isopropyl alcohol slightly changed the dye degradation indicating that $OH\cdot$ radicals were minor factors in the photocatalytic degradation process, whereas the addition of h^+ capture (EDTA-2Na) caused a great decrease in the degradation efficiency as shown in Fig. 10. This foundation distinctly denoted that positive holes are the major active species of the dye dissociation.

Supplementary Files

This is a list of supplementary files associated with this preprint. Click to download.

- [Supplementrymaterials.doc](#)